Construction and Building Materials 319 (2022) 126124

Contents lists available at ScienceDirect

Construction and Building Materials

journal homepage: www.elsevier.com/locate/conbuildmat

High strength fiber reinforced one-part alkali activated slag composites from industrial side streams

Priyadharshini Perumal [a,*], Hoang Nguyen [a], Valter Carvelli [b], Paivo Kinnunen [a], Mirja Illikainen [a]

[a] Fibre and Particle Engineering Research Unit, University of Oulu, Pentti Kaiteran katu 1, 90014 Oulu, Finland
[b] Department A.B.C., Politecnico di Milano, Piazza Leonardo Da Vinci 32, 20133 Milan, Italy

ARTICLE INFO

Keywords:
Steel fiber
Mineral fiber
One-part alkali activated material
High strength composites
Numerical analysis

ABSTRACT

This paper details the effect of fiber reinforcement on mechanical characteristics of by-products based one-part alkali activated material (AAM). Two different binder matrices were considered in this study, such as, plain slag, and ternary blended slag, to understand their efficiency in fiber reinforced system. These matrices were reinforced with 1% v/v of three different fibers (steel, glass and basalt) to improve the flexural performance of high strength mortar blends. Steel fiber reinforced one-part AAM outperforms mineral fibers in compressive strength contribution. The fracture energy of steel fiber reinforced compositions was roughly 4 times higher than that of mineral fiber reinforced materials. In addition, the flexural performance of ternary blended matrix was higher than that of slag-based composition regardless fiber types and properties. Finally, preliminary finite element modelling was considered to assess the applicability of the concrete damage plasticity constitutive model in predicting the nonlinear behavior of the developed composites. The numerical predictions proved the accuracy of the model with good agreement between experimental and numerical results.

1. Introduction

Alkali activated materials are alternative binders to the traditional Portland cement composites which facilitates the use of industrial by-products such as fly ash and various slags. Alkali activates the aluminosilicates present in the precursors from industrial side streams and forms dense polymeric gels resulting in high strength and durability properties [1–3]. Evidently, AAMs are potential replacement for conventional cement binders stating their ecological low energy consumption and greenhouse gas emissions [4]. However, the practical application of AAM in industrial scale is limited since the liquid alkali activators are corrosive and causes serious issues in handling, mixing and transportation [5]. Additionally, curing condition is another concern where most of the low calcium AAM needs heat treatment for the strength development [6,7]. To curtail the mentioned problems about AAMs, solid alkali is premixed with the aluminosilicate materials which can be activated just by adding water and termed as one-part AAM [8,9]. Some of the industrial side streams like blast furnace slag (BFS) enables room temperature curing, making the process easier to adopt in larger scale in-situ applications [10,11].

Several studies have shown high strength of such one-part AAM with fly ash and BFS as aluminosilicate precursors and, sodium silicate and/or sodium hydroxide as solid precursors [5,10–12]. Like any other concrete material, tensile behavior of high strength one-part AAMs are not on par with their performance for compressive one [13]. In such cases, fibers come as an effective addition to attenuate the brittle failure and improve the pseudo strain hardening behavior of the high strength matrices [14–16]. Reinforcing the one-part AAMs with fibers improves the mechanical performance and toughness of matrix by delaying the cracks initiation and propagation. The bridging action of fibers controls the crack growth until fiber fails locally by debonding, sliding and pull-out [17]. This extends the energy needed for crack propagation and improves the post-crack behavior which positively affects the strength, toughness, and durability of the material ADDIN CSL_CITATION [18–20]. It is even proven that fiber reinforcement helps in reducing the environmental impact of the AAM by contributing comparable properties of conventional material at lower alkali dosage [21]. These benefits of fiber reinforcement in AAM with different types of fiber, such as, polyvinyl alcohol (PVA) [22–24], polypropylene (PP) [15,23,25], polyethylene (PE) [26], glass [21,24,27], steel [21,23–25], basalt

* Corresponding author.
E-mail address: priyadharshini.perumal@oulu.fi (P. Perumal).

https://doi.org/10.1016/j.conbuildmat.2021.126124
Received 31 August 2021; Received in revised form 3 December 2021; Accepted 15 December 2021
Available online 23 December 2021

Table 1
Chemical composition (wt%) of binder material.

Oxide	CaO	SiO_2	Al_2O_3	Fe_2O_3	MgO	SO_3	Others
GGBFS	38.51	32.33	9.58	1.23	10.24	4.00	4.11
Silica fume	0.78	94.25	0.23	0.84	0.18	0.13	3.59
Phyllite dust	9.01	71.91	8.96	2.07	2.06	0.26	5.73

[25,28], carbon [29], and several vegetable-based fibers such as, sisal, cotton and so on [30,31], are well established in the existing literature. However, the benefits of fiber addition depend on various factors such as type, aspect ratio of fibers and mix composition [32]. For example, Guo and Pan found that steel fibers provide the reinforcing effects whereas, PP and basalt fiber contributes to the long-term mechanical properties in a fly ash – slag AAM [25]. Considering the vegetable fibers in AAM, the need for further development about fiber treatment to withstand the aggressive alkaline environment without affecting the matrix- fiber bonding, is emphasized [30]. There are several opportunities in this area to explore about the utilization of fibers in AAM for structural, environment and cost benefits.

The present study is encouraged by the lack of knowledge existing in high strength one-part AAM with blended binders. Though there are few studies reporting about the effect of fiber reinforcement in one-part AAMs [16,33–35], this is the first attempt to measure the mechanical effect of fiber incorporated in blended binders involving one-part AAMs. Hence, this study gives a contribution, by experimental measurements and numerical modelling on understanding the effect of metallic (steel) and mineral (glass and basalt) fibers on some mechanical properties of one-part AAM with ternary blended binder composition and different industrial side streams (BFS, silica fume and phyllite dust). The numerical model was able to predict the complete macroscopic behavior of the reinforced composites as well as the evolution of the damage.

2. Materials and methods

2.1. Materials

Ground granulated blast furnace slag (GGBFS) was obtained from Finnsementti (Finland) and sodium silicate ($SiO_2/Na_2O = 0.9$) as 1 mm sized granules from Alfa Aesar (Germany). One-part alkali binder mix was prepared by co-grinding (GGBFS) with anhydrous sodium metasilicate in a ball mill (Germatec, Germany) for 30 min. Particle size distribution was then analyzed through laser diffraction (Beckman Coulter 13 320) and co-grinding of slag resulted in a median particle size d_{50} value as 9.75 μm. Milled Silica fume (Parmix-silika, Fescon Ltd., Finland) of d_{50} 23.21 μm and phyllite dust (powder waste from local tiles manufacturing, Finland) of d_{50} 196.77 μm were used as co-binders to achieve high packing density by applying modified Andreasen model [36,37]. Chemical composition of different binder materials was analyzed by X-ray fluorescence (XRF, PANalytical Axiosmax) at 4 kV (see Table 1).

Standard sand, according to DIN EN 196-1 (passing 2 mm, density: 2.67 g/cm^3), from Normensand (Germany) was used as fine aggregate. Moisture content of the sand was < 0.2%. Water absorption and fineness modulus were calculated as 0.57% and 2.93, respectively. In this study, steel fibers (6 and 12 mm length), glass fiber, basalt fiber were used to produce fiber reinforced one-part alkali activated mortar. Table 2 lists the mechanical and physical properties of these fibers. Steel fibers were supplied by Weidacon (Germany). Glass fiber with very high chemical resistance was provided by Owens Corning (USA). Basalt fibers were manufactured by Basaltex (Belgium) which can withstand high temperature and harsh environment. A common fiber length of 6 mm was chosen to help in better comparison between different types of fiber used. Influence of fiber length was studied in steel fibers with S-6 and S-12 (Table 2).

Lignosulphonate (WRDA 90D, GCP, UK) with 30% solid content was used as a superplasticizer as in [38] being the best performing in one-part alkali-activated materials, especially for slag composition.

2.2. Mortar mix design and preparation

Based on preliminary studies and earlier research [33,34], 1% (volume) of fibers was considered suitable to improve the mechanical properties. The contents refer to the volume of fibers incorporated in the volume of one-part alkali activated mortar (AAM). Table 3 lists the 12 different mix compositions produced for this study. Two types of binder with co-grinded slag (with 10% sodium silicate) were used. Binder G1 contains only the co-grinded slag, whereas G2 is a ternary blend with co-grinded slag, silica fume and phyllite dust. G1 acts as control reference mix whereas, composition of G2 binder was determined based on

Table 2
Mechanical and physical properties of fibers.

ID	Type	Young's modulus (GPa)	Elongation at break (%)	Tensile strength (MPa)	Length (mm)	Diameter (mm)	Density (kg/m^3)
S-6	Steel	200	3	1300	6	0.16	7870
S-12	Steel	200	3	≥2200	12	0.13	7886
G-6	Glass	72	4.9	1000–1700	6	0.014	2680
B-6	Basalt	100	3.1	4100–4500	6	0.018	2650

Table 3
Mix composition of fiber reinforced one-part AAM.

Mix ID	Binder content (g)			Fine aggregate(g)	Fiber content (g)				SP(g)	Water content(g)
	Co-grinded slag	Phyllite dust	Silica fume		Steel		Glass	Basalt		
					S-6	S-12	G-6	B-6		
G1	742.8	–	–	1257.1	–	–	–	–	7.4	222.8
G1S-6	742.8	–	–	1257.1	72	–	–	–	7.4	222.8
G1S-12	742.8	–	–	1257.1	–	72	–	–	7.4	222.8
G1S-M	742.8	–	–	1257.1	36	36	–	–	7.4	222.8
G1G-6	742.8	–	–	1257.1	–	–	25	–	7.4	222.8
G1B-6	742.8	–	–	1257.1	–	–	–	24.5	7.4	222.8
G2	514.2	57.1	114.2	1257.1	–	–	–	–	7.4	205.7
G2S-6	514.2	57.1	114.2	1257.1	72	–	–	–	7.4	205.7
G2S-12	514.2	57.1	114.2	1257.1	–	72	–	–	7.4	205.7
G2S-M	514.2	57.1	114.2	1257.1	36	36	–	–	7.4	205.7
G2G-6	514.2	57.1	114.2	1257.1	–	–	25	–	7.4	205.7
G2B-6	514.2	57.14	114.29	1257.1	–	–	–	24.5	7.4	205.7

Table 4
Molar ratios of the designed binder composition.

Binder type	SiO_2/Al_2O_3	Na_2O/SiO_2	Na_2O/Al_2O_3	CaO/SiO_2	Na_2O/H_2O
G1	6.705	0.155	1.041	1.090	0.052
G2	5.765	0.011	0.062	0.058	0.060

particle packing method to achieve ultra-high strength [37]. Binder to aggregate ratio and water to binder ratio were maintained constant at 0.6 and 0.3, respectively. Table 3 gives the content of the different material components. Superplasticizer (SP, 1% binder weight) was used to ensure proper workability and fiber dispersion in the matrix. Molar ratios of the designed binder compositions (G1 and G2) are listed in Table 4. It is worth to note that the binder G2 has lower ratio of Na_2O/SiO_2 compared to the binder G1. This is due to the reduced amount of co-grinded slag in G2 which ultimately resulted in the reduction of activator content (solid sodium silicate).

Dry ingredients (binder and fine aggregate) were mixed in a 5-liter Kenwood mixer at a low (70 rpm) and high (150 rpm) speed for a minute each. Part of the water was added at this stage, while the mixing was continued in low speed and superplasticizer was introduced with the remaining portion of the water at later stage. A high-speed mixing was used for further 2 min to result in a homogeneous mortar. As a final step, fibers were introduced by gradually addition to the fresh mortar while stirring in low speed to avoid balling effect. Fresh fiber reinforced one-part AAM was then cast into prismatic molds. The specimens were cured in a humidity chamber at 20 °C and 100% RH until testing. For each mix composition (Table 3), six prismatic beams were cast, total of 72 specimens. The mix ID in Table 3 contains: the binder ID (G1 or G2), the fiber material and diameter (S-6 or S12, G-6, B-6). As for the steel fibers, S-M indicates a hybrid reinforcement containing the same content of S-6 and S-12 (1:1).

2.3. Experimental procedures

The influence of different fiber types on some mechanical properties was measured after 28 days of curing age. Fracture toughness was estimated by bending of notched beam as per RILEM recommendation 1985 TC50-FMC [39]. Fig. 1 shows the test set up and dimensional details of the notch of 1 mm width. The three-point bending of notched beams was displacement controlled (0.4 mm/min). Fracture energy and toughness were calculated as discussed in [40]. The two halves of the tested beam were used for compressive strength measurement with displacement control at 2 mm/min, loading a surface of 40x40 mm^2.

Digital image correlation (DIC) technique was used together with flexural tests for notched beams to monitor the crack propagation. Images were captured by two high-speed camera with a LED light and analyzed by LaVision StrainMaster software [41]. The frequency of image acquisition was 1 Hz, while the aperture and the shutter speed of camera were set to f/4.0 and 1500 μs, respectively. The samples' surface was prepared with speckle pattern including white background and randomly distributed black dots (Fig. 1b). The post processing of images allows to measure crack mouth opening displacement (CMOD) and crack evolution. Some of the adopted parameters for DIC were subset, size 37 and step size 3.

3. Experimental results and discussions

The measurements and observations from experimental results helped in composing an overview of the effect of different fibers on the strength characteristics of the fiber reinforced alkali activated mortar (FR-AAM). Flexural behavior of notched FR-AAM specimens provided considerable information on the effect of the fibrous reinforcement, which was well documented with the help of DIC technique. Crack initiation and propagation were monitored, and fracture surface was observed through scanning electron microscope (SEM) to understand the failure pattern of different fibers with G1 and G2 mixes. Flexural as well as compression loadings confirmed the better performance of steel fibers compared to mineral ones in improving the strength characteristics of FR-AAM.

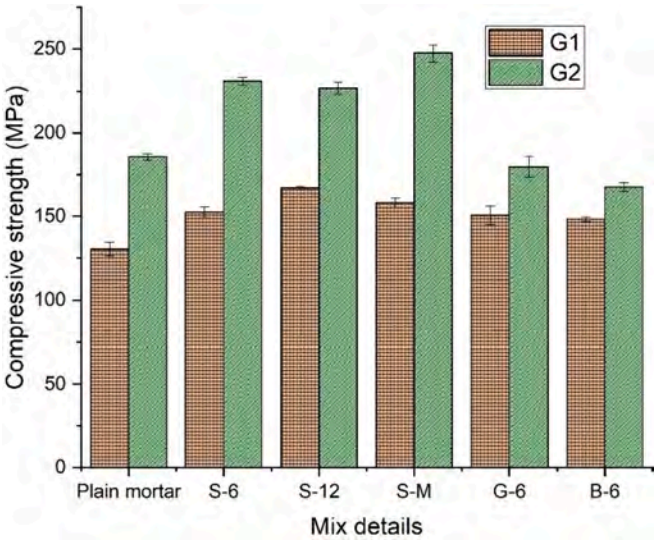

Fig. 2. Compressive strength of AAM after 28 days of curing.

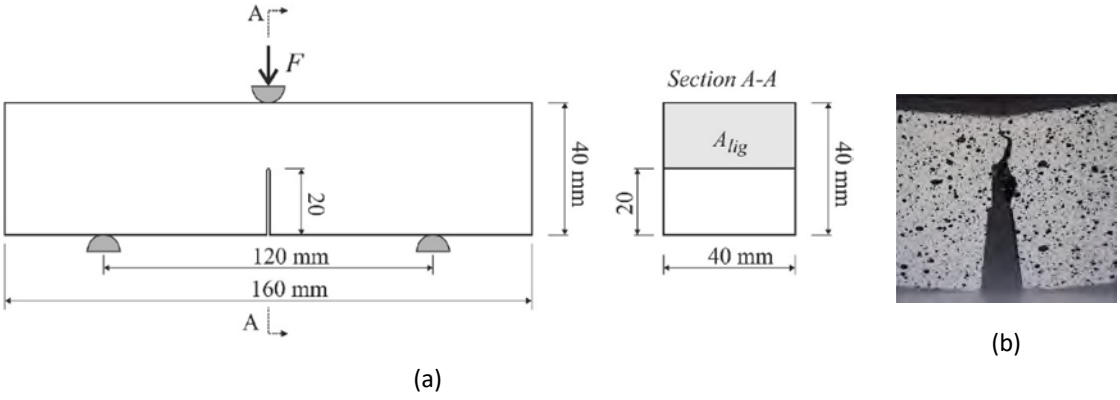

Fig. 1. (a) Fracture toughness test setup for notched beam [27], and (b) representative crack propagation in a notched (G1S-12) sample after testing.

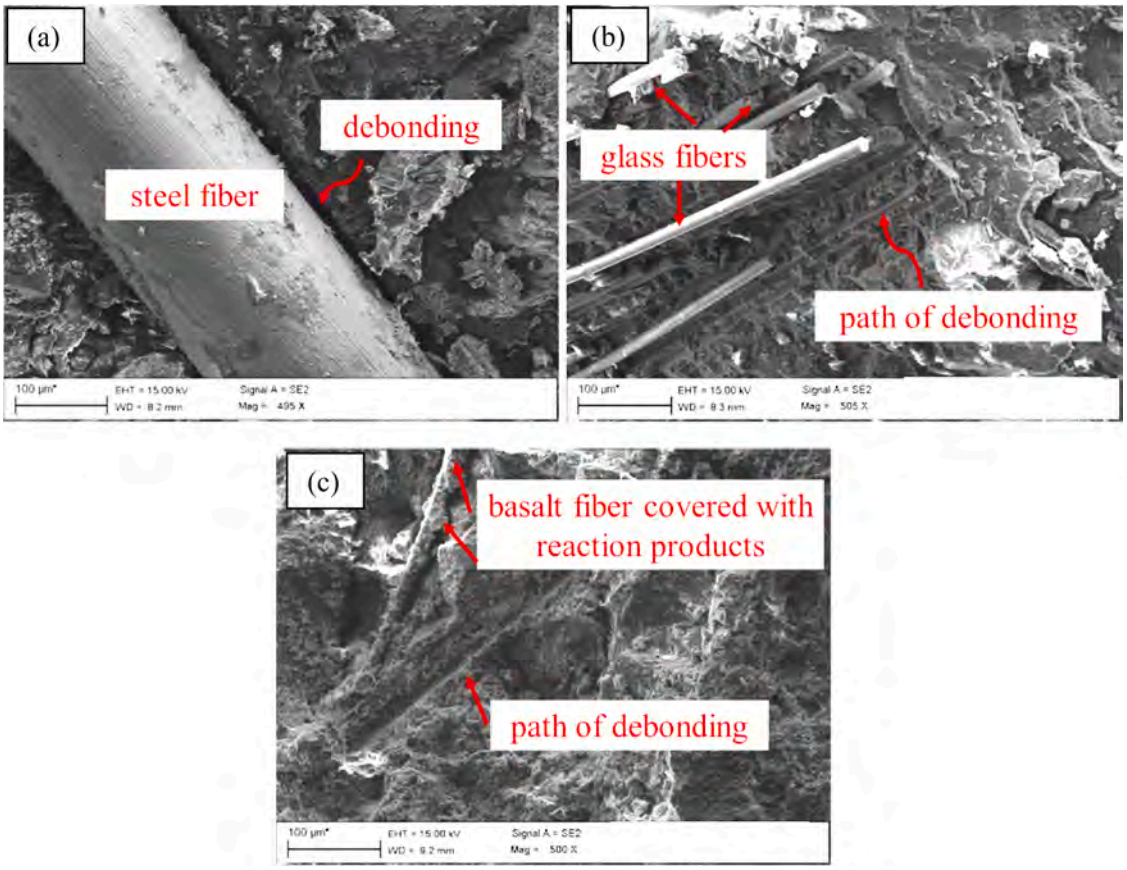

Fig. 3. Representative microstructure of fibre reinforced one-part AAM (G1).

3.1. Unconfined compression

AAM with ternary blended binder matrix (G2) resulted in strength improvement compared to the sole binder (G1) matrix with co-grinded GGBFS. Fig. 2 shows a strength improvement of approximately 38% with the combination of co-grinded slag, silica fume and phyllite dust. It is interesting to note that, regardless of the lower dosage of activator content (Table 3 and Table 4), G2 mixes outperformed G1 mixes (Fig. 2). It was established that addition of silica fume helped polycondensation and formation of cross-linked calcium alumina-silicate hydrates (C-A-S-H) and sodium alumina-silicate hydrates (N-A-S-(H)) which improves the strength properties [37]. Phyllite dust acted as a filler material and a nucleation site to enhance hydration reactions. Ternary blended mix, thus given the best compressive strength results among the plain alkali activated mortar.

Irrespective of the type of binder matrix, the compressive strength increased by 15% to 30% with the inclusion of steel fibers. In recent publications, similar strength improvement with steel fiber reinforced AAM was reported in one-part systems [33,35]. Though, this is contradicted in two-part AAM concrete studies indicating a strength loss with fiber addition [42]. Length of fiber is an important factor affecting the strength properties and made a 13% substantial strength enhancement in the G1 mix. It was also the case with binary blended two–part alkali activated slag mortar at high fiber dosages [14]. However, in G2 mix, there is no significant strength difference between short (S-6), long (S-12) fiber. A microstructural representation of G1 and G2 matrix with steel fiber (S-12) reinforcement is shown in Fig. 3a and 4a, respectively. Debonding failure of fibers is noted in both G1 and G2 matrix with some observation of pull out effect on G2 matrix. The residual mortar adhered to the fibers shows the effective bonding between the fibers and the mortar. A better performance of steel fibers is also notable with the combination of the two fiber lengths (1:1, short and long fibers). It resulted in an average ultra-high strength of 242 MPa in G-2 matrix (G2S-M) which is 33% higher than the plain AAM (G2, 180 MPa).

Considering the fiber type, steel fiber outperformed the glass and basalt fibers in contribution to compressive strength. With single binder system, inclusion of glass or basalt fibers resulted in an approximate strength increase of 15%. However, blending of three binders in ternary system (G2) caused a slight strength loss with mineral fibers from 2% to 8% (See Fig. 2). This can also be due to the influence of the binding system in the effective dispersion of fibers. It is observed that cluster of glass (Fig. 3b and 4b) and basalt (Fig. 4c) fibers are still bonded together in the binder matrix, explaining the inefficient fiber distribution. Additionally, basalt is known to be unstable in the high alkaline environment causing the deterioration of the fiber itself [43]. SEM image of basalt reinforced AAM shows a clear evidence of its reactivity with the matrix and the fibers are entrapped into the reaction products (Fig. 3c and 4c). This explains the strength loss with basalt fibers reinforcement in the alkali activated systems, and motivates the need for alkali resistive coating [33,35,44].

3.2. Flexure of notched specimens

The steel fiber reinforcement had excellent load carrying capacity, and the fiber length plays an important role in the post-peak behavior of materials. Fig. 5 shows the average load vs. CMOD curves of all mix compositions. The CMOD was measured by the DIC technique during loading. It clearly shows that the plain materials (i.e., G1 and G2) had typical brittle failure under a mode I fracture. Notably, G2 had higher peak load than G1, which is in-line with the comparison in compressive strength between these two mixtures. The steel fibers significantly improved the peak load and post-peak branch of all compositions. Steel fiber-reinforced G2 mixtures attained higher peak load than that of G1 with the same type of reinforcement. Reasons are the higher strength of

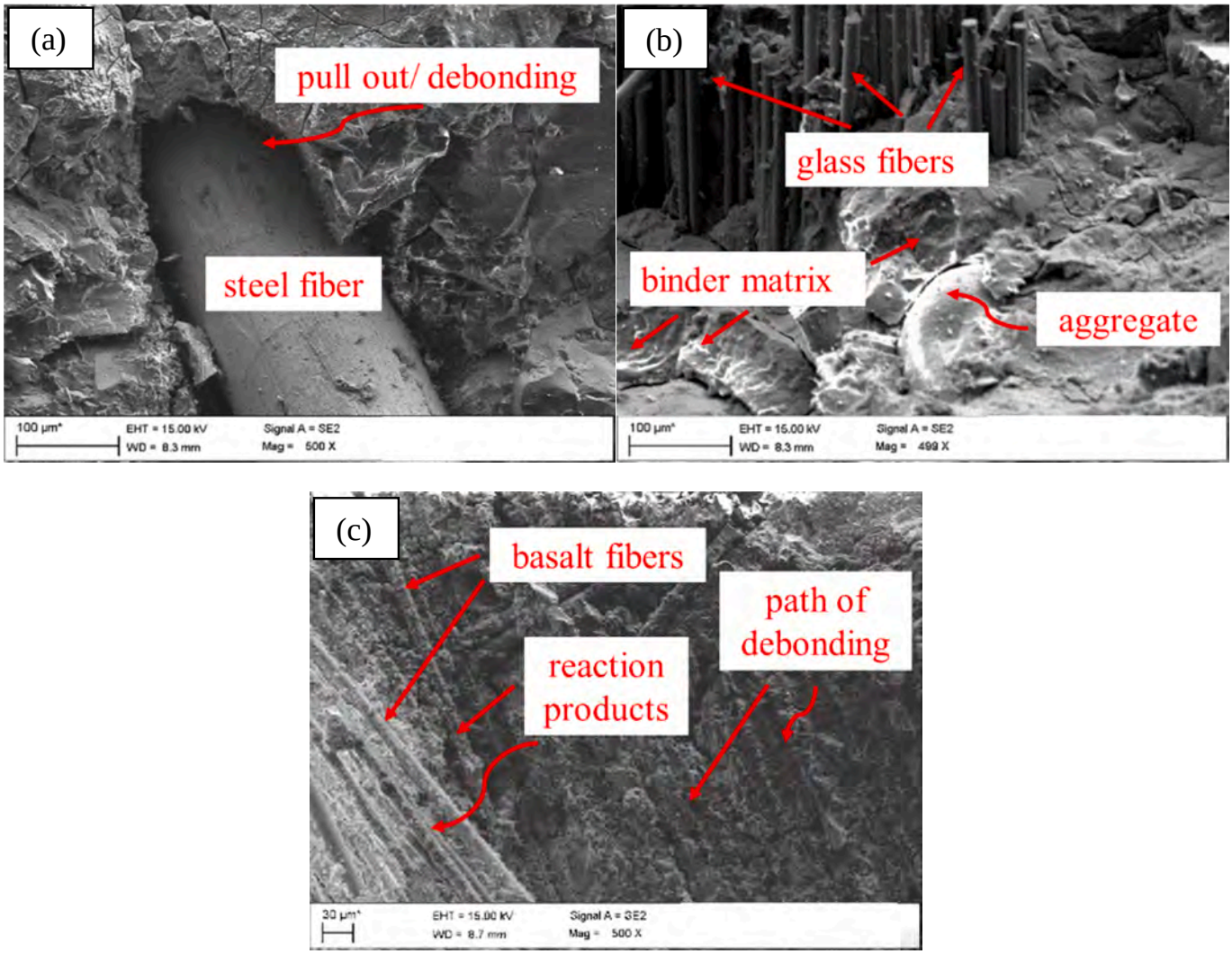

Fig. 4. Representative microstructure of fibre reinforced one-part AAM (G2).

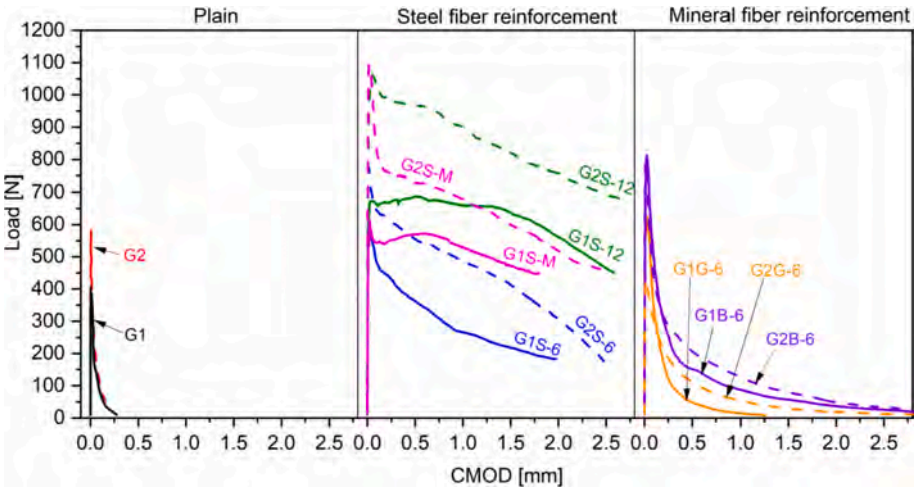

Fig. 5. Average load vs. CMOD curves of all mixtures under mode I fracture test.

G2 matrix than G1, and the better interfacial bond between matrix and fibers of G2 than that of G1, leading to higher load carrying capacity. All the mix compositions exhibited softening post-peak branch, in which the length of steel fibers strongly affected the reduction rate in load level. For instance, in the same G2 matrix at CMOD = 2.0 mm, the load level of G2S-6 (6-mm long fiber), G2S-M (hybrid of 6- and 12-mm fiber), and G2S-12 (12-mm fiber) were approximately 315, 520, and 760 N, respectively. The latter was 2.4 times higher than the former. A similar

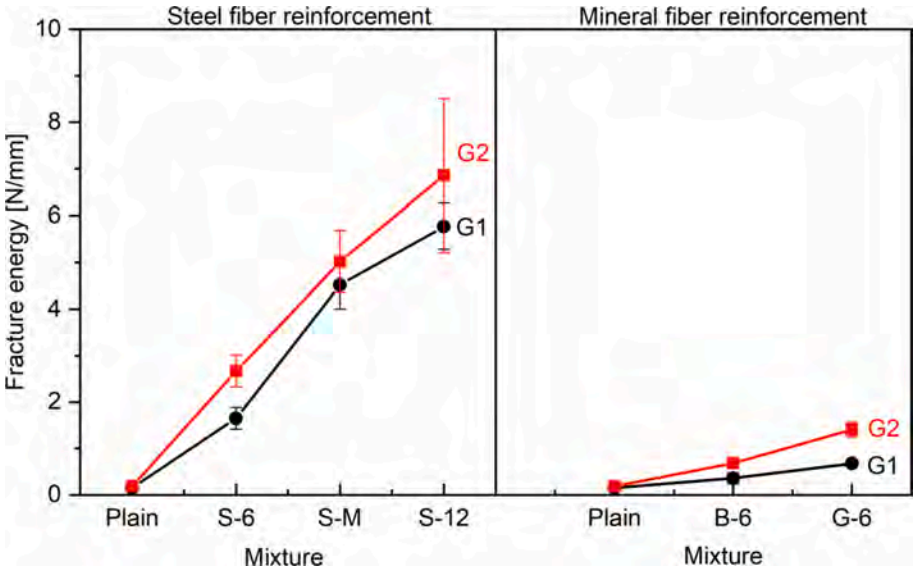

Fig. 6. Fracture energy of all mixtures at failure.

performance was also observed in G1 matrix (Fig. 5).

In contrast, the mineral fibers exhibited poor load transferring between the fibers and matrices compared to the steel fiber-reinforced compositions. Although both glass and basalt fibers enhanced the peak load of the composites, there was little improvement for post-peak branch, in which all compositions showed quasi-brittle behavior. This can be attributed to high pH environment that led to partially dissolve mineral fibers [45,46], and the poor distribution of the mineral fibers in the matrices that limited the contribution of the fibrous reinforcement to the composites (see SEM images in Fig. 4). These factors eventually caused less efficiency in the load transferring capacity between the mineral fibers and the matrices.

Fracture energy was increased in all reinforced compositions, but the effect was only clearly observed on steel fiber-reinforced composites. Fig. 6 shows the fracture energy of all mixtures, in which the materials were divided into 2 groups: steel fiber and mineral fiber reinforcement. It is clearly seen that the steel fibers contributed to energy absorption much better than mineral fibers. The highest fracture energy was account for G2S-12 with 6.8 N/mm, which was around 4 times higher than that of G2G-6 (fracture energy 1.4 N/mm at failure). Note that the fracture energy of all reinforced mixes was higher than that of plain materials, which were only 0.15 and 0.18 N/mm for G1 and G2, respectively. There was a proportional relationship between the energy absorbed in steel fiber-reinforced composites with the fiber length. The long steel fiber is more favorable to enhance the fracture energy of the material due to better fiber bridging action [47,48]. Notably, the steel fiber reinforced G2 generally attained higher fracture energy at failure compared to the same fiber types in G1 matrix. However, the difference was not statistically significant. In contrast, composites from G2 matrix worked better with glass and basalt fibers in comparison to G1 matrix. Additionally, glass fiber obtained higher fracture energy than basalt fiber in both matrices (Fig. 6). This can be due to the better alkali resistance of glass fiber.

4. Numerical modelling

To reduce expensive and time-consuming experimental measurements, predictive models are necessary to estimate the mechanical response in any loading condition, and for the proper modeling of the material behavior in structural analyses. For the composites under consideration, preliminary numerical predictions were performed assuming constitutive models and theoretical assumptions available in

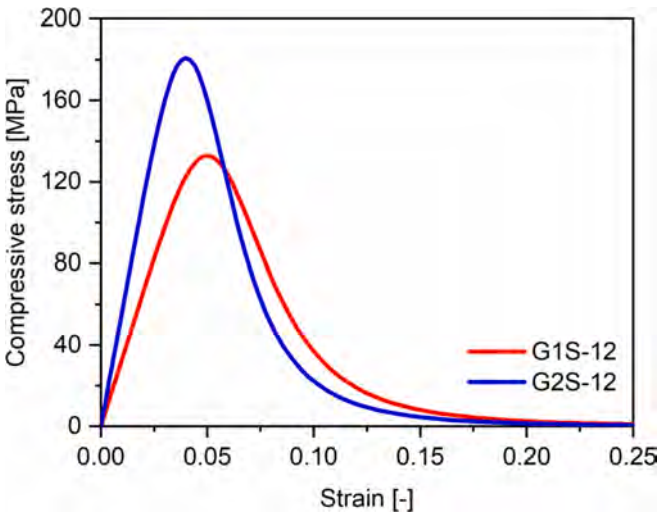

Fig. 7. Estimated compressive cylindrical stress vs. strain behavior.

the literature and codes for concrete structures. The peculiar mechanical features of the considered materials allowed to adopt an available constitutive model implemented in the finite element code Abaqus [49]. The Concrete Damaged Plasticity (CDP) is suitable for homogeneous isotropic materials having different tensile and compressive behavior, and it includes the modelling of the damage initiation and development. Hence, this can consider the features of the considered composites, once the proper input paraments are identified. The numerical model accuracy was assessed replicating the experimental three-point bending test of notched specimen for fracture toughness measurement of two representative materials G1S-12 and G2S-12 (see Table 3).

As for the input parameters of the CDP model, some assumptions and approximations were introduced, due to unavailable experimental measurements, mainly for post peak compression and tensile behavior. The dilation angle ψ was adopted to be 40°, being in the typical range 30°÷45°. As suggested in [49], the flow potential eccentricity was assumed ϵ=0.1, the ratio of initial equibiaxial compressive yield stress to initial uniaxial compressive yield stress was set $\sigma_{b0}/\sigma_{c0} = 1.16$, the ratio of the second stress invariant on the tensile meridian to that on the compressive meridian was set $K_c = 0.67$, and viscosity parameter $\mu = 0$.

The experimentally measured average uniaxial cubic compression

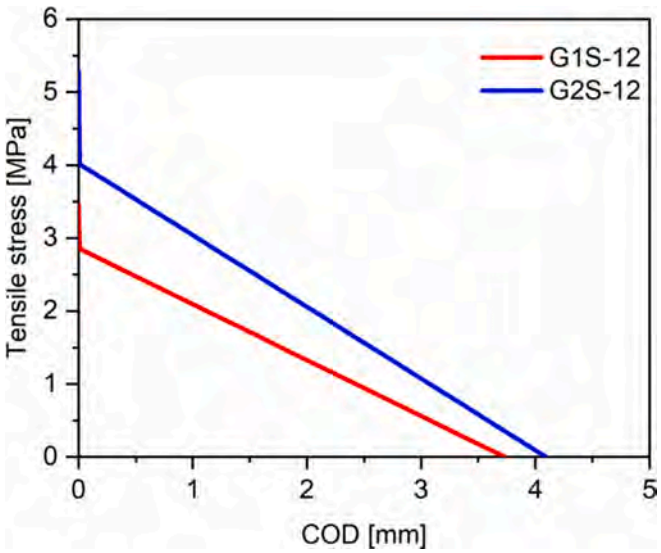

Fig. 8. Estimated bi-linear post-peak stress vs. crack opening displacement.

strength σ'_c (see Fig. 2) was adopted to build the cylindrical stress (σ_c) vs. strain (ε) diagram, depicted in Fig. 7, according to the relationship proposed in [50]:

$$\sigma_c = \sigma'_c \frac{\beta\left(\frac{\varepsilon}{\epsilon'_c}\right)}{\beta - 1 + \left(\frac{\varepsilon}{\epsilon'_c}\right)^{\beta}} \quad (1)$$

where

$$\beta = \frac{1}{1 - \frac{\sigma'_c}{\epsilon'_c E_c}} \quad (2)$$

In eqns. (1, 2), ϵ'_c is the strain corresponding to σ'_c , E_c is modulus of elasticity and β is a material parameter mainly defining the descending branch. An iterative numerical procedure allowed to set the parameter β = 5, quite typical for high strength concretes [50]. Then, the modulus of elasticity was estimated by eqn. (2) as 3317 MPa and 5647 MPa for G1S-12 and G2S-12, respectively, while Poisson's ratio was set 0.2.

The tensile behavior of material was not experimentally measured. Therefore, the tensile strength was estimated by the maximum load of the notched three-point bending tests, while the complete tensile constitutive behavior was considered linear up to the tensile strength, whereas bi-linear post-peak stress vs. crack opening law was estimated according to the proposal in [51], as adopted in [52], being aware that more complex models are available for cementitious fiber reinforced materials (see e.g. [53].

The indirect tensile strength was estimate from the flexural tensile strength as suggested in [54], getting 3.45 MPa and 5.28 MPa for G1S-12 and G2S-12, respectively.

As for the bi-linear post-peak tensile stress vs. crack opening displacement, the first branch was modeled following the model code 2010 [54] for plain concrete. The second branch was estimated as detailed in [51], which was dedicated to steel fiber-reinforced concrete. This second linear portion was obtained considering the post-cracking residual strength f_{R1} and f_{R3} at COD of 0.5 mm and 2.5 mm, respectively, as for the experimental tests (see Fig. 5). By adopting parameter $k_a = 0.37$ and shifting the value of $f_{Fts} = k_a \bullet f_{R1}$ (serviceability residual strength) at zero crack opening [51], the first point of the second linear branch was defined. Another point of the second linear branch was estimated as $f_{Ft,2.5} = 0.5 f_{R3} - \frac{k_b}{2} f_{R1}$, where $k_b = 0.529 - 0.143 \frac{f_{R3}}{f_{R1}}$. Finally, the complete tensile stress vs. crack opening displacement curve (see Fig. 8) was fully defined by the intersection point of the first and the second branches, which was implemented in the numerical model.

The shape of the notched three-point bending specimen depicted in Fig. 1 was considered for the finite element discretization. The specimen was constrained to fulfill the experimental supports, namely, no displacement ($u_x = u_y = 0$) of nodes on the bottom surface line reproducing one support, and no displacement in the vertical direction ($u_y = 0$) of nodes on the line simulating the other. While an increasing vertical displacement (u_y) was applied on the top surface mid span center line (Fig. 9).

The specimen was discretized by 3D solid hexahedral elements C3D8R, with reduced integration. Finite element mesh had increasing density from the sides to the center to get the maximum density approaching the crack tip and the mid span compressed zone where the average length of element side was approximately 0.4 mm (Fig. 9). The total number of elements was 93840. The latter resulted from a mesh sensitivity analysis to balance simulation time and accuracy of the

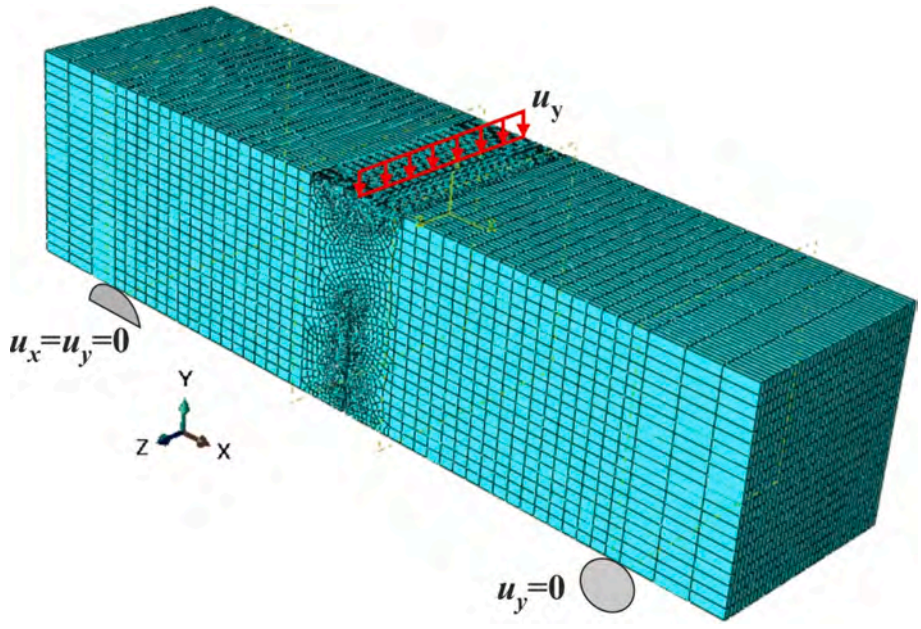

Fig. 9. FE mesh and boundary conditions of the notched three-point bending test.

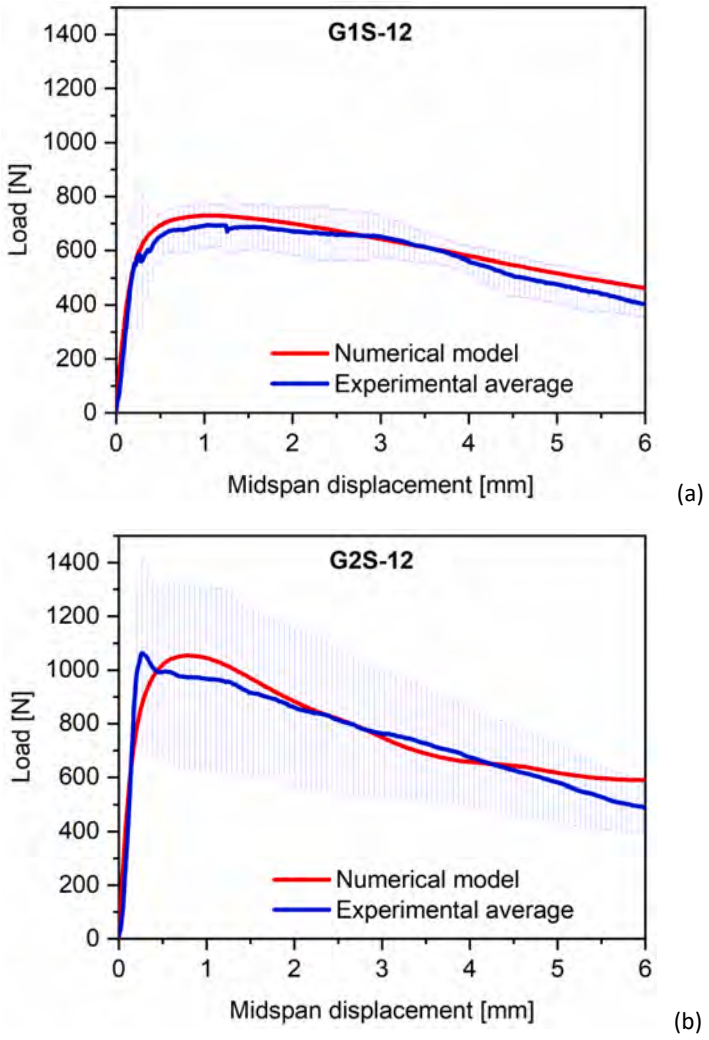

Fig. 10. Comparison of the average experimental (error bars represent the standard deviation of three tests) and numerical model load vs. mid-span deflection of (a) G1S-12 and (b) G2S-12.

outcomes.

The accuracy of the numerical model was verified in simulating the fracture toughness test of the two considered reinforced composites. Results are compared to the average experimental (three tests) load-midspan deflection curves in Fig. 10.

Overall, the numerical simulations can be considered satisfactory having a good agreement with the average experimental measurements, with some discrepancies in predicting the peak load and the post-peak of load-midspan deflection trend. Nevertheless, the numerical model demonstrated the capacity to predict, to some extent, the complete behavior of the material under the considered load condition, with proper estimation of the damage evolution also under post peak conditions when reinforcement has the main role. This was assessed comparing the numerical predicted damage pattern at the maximum midspan displacement (see Fig. 10), which should represent the cracks configuration as observed during experimental loading. The maps of the predicted equivalent plastic strain magnitude, over the full height central portion of the specimen, are detailed in Fig. 11, beside the experimental DIC estimation of the max principal strain.

Hence, considering the assumptions adapted from codes and models dedicated to steel fiber-reinforced concrete, and the approximations of the materials parameters, the CDP constitutive model can numerically predict the overall quasi-static response of the considered reinforced one-part alkali activated slag composites. The accuracy can be improved when accurate experimental measurements are available for the compression and tensile post-peak response.

5. Conclusions

The study was focused on the performance of fiber reinforced alkali activated slag composites with three different fibers such as, steel, glass, and basalt. A ternary blended matrix was also introduced to compare with plain slag mix, to understand the influence in the presence of different fibers.

The main understanding from the outcomes of the experimental study is summarized here:

- Ternary blended matrix had strong interaction with fibers in addition to their contribution in optimized particle packing which is reflected in the better strength properties.
- Steel fibers outperformed other type of fibers in the alkali activated slag composites. Longer the fiber the better was the load carrying capacity which was in the order of 12 mm > Mixed (12 mm + 6 mm) > 6 mm length of fibers. Similar trend was observed also in fracture energy measurements.
- Mineral fibers (glass and basalt) were unstable in high alkaline environment, resulting in strength loss.

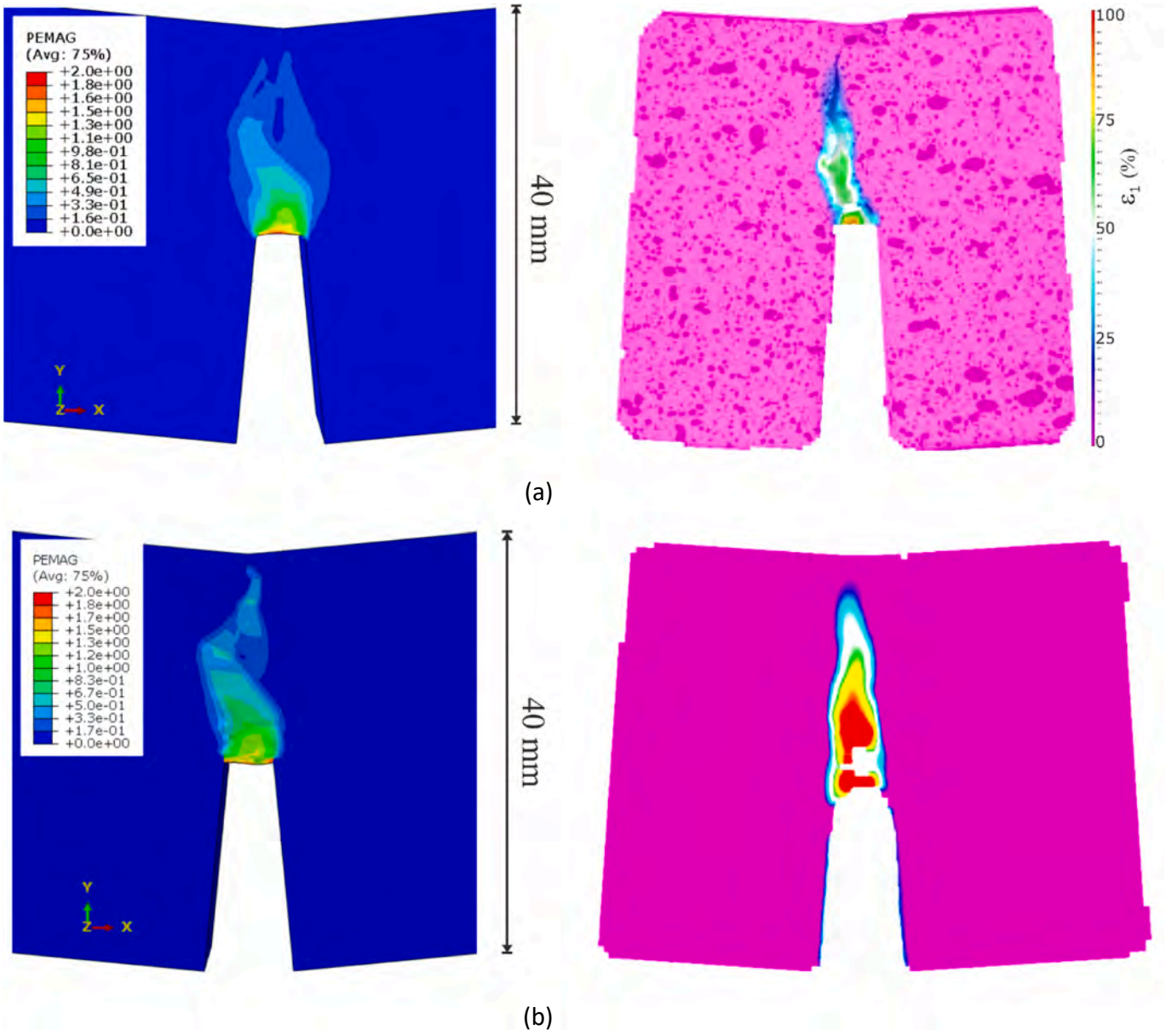

Fig. 11. Maps of the predicted equivalent plastic strain magnitude (PEMAG) (left) and experimental max principal strain by DIC (right) of (a) G1S-12 and (b) G2S-12.

Based on the experimental findings, two slag composites (plain and ternary blend) with 12 mm steel fibers were chosen to be studied for the numerical model. For the present study, concrete damaged plasticity (CDP) model was adopted in modelling the damage initiation and development. The proposed model demonstrated to have good accuracy and capacity to predict the complete behavior of the material under the considered loading conditions when reinforcement has the main role. However, a better accuracy is expected with the complete measurements of the post-peak behavior of the material.

Overall, it was shown from the study that ternary blended slag composites with steel reinforcement results in high load carrying capacity (compressive strength 242 MPa). Nevertheless, further investigations need addressing, such as understanding the micro level damage mechanisms and durability issues for the designed high strength composites.

CRediT authorship contribution statement

Priyadharshini Perumal: Conceptualization, Methodology, Validation, Formal analysis, Investigation, Visualization, Writing – original draft, Writing – review & editing, Project administration. **Hoang Nguyen:** Conceptualization, Validation, Investigation, Writing – original draft. **Valter Carvelli:** Visualization, Validation, Formal analysis, Investigation, Writing – original draft. **Paivo Kinnunen:** Conceptualization, Funding acquisition, Supervision, Writing – review & editing. **Mirja Illikainen:** Funding acquisition, Supervision, Writing – review & editing.

Declaration of Competing Interest

The authors declare that they have no known competing financial interests or personal relationships that could have appeared to influence the work reported in this paper.

Acknowledgements

The authors gratefully acknowledge the financial support received from the project GEOMINS [grant ID: 319676]. The authors would like

to thank laboratory staff, Elisa Wirkkala and research trainee, Eemeli Tapalinen for the contributions to the laboratory work. P.P. gratefully acknowledges the financial support received from the European Union's Horizon 2020 research and innovation programme under the Marie Skłodowska Curie grant agreement No [839848].

References

[1] J. Payá, J. Monzó, M.V. Borrachero, M.M. Tashima, Reuse of aluminosilicate industrial waste materials in the production of alkali-activated concrete binders, Woodhead Publishing Limited, 2015. Doi: 10.1533/9781782422884.4.487.
[2] J.L. Provis, Alkali-activated materials, Cem. Concr. Res. 114 (2018) 40–48, https://doi.org/10.1016/j.cemconres.2017.02.009.
[3] J.L. Provis, Alkali activated materials: State of The Art Report, Springer Singapore, New York, 2014.
[4] P. Duxson, A. Fernández-Jiménez, J.L. Provis, G.C. Lukey, A. Palomo, J.S.J. van Deventer, Geopolymer technology: The current state of the art, J. Mater. Sci. 42 (9) (2007) 2917–2933, https://doi.org/10.1007/s10853-006-0637-z.
[5] B. Nematollahi, J. Sanjayan, F.U.A. Shaikh, Synthesis of heat and ambient cured one-part geopolymer mixes with different grades of sodium silicate, Ceram. Int. 41 (4) (2015) 5696–5704, https://doi.org/10.1016/j.ceramint.2014.12.154.
[6] A. Heath, K. Paine, M. McManus, Minimising the global warming potential of clay based geopolymers, J Clean Prod 78 (2014) 75–83, https://doi.org/10.1016/j.jclepro.2014.04.046.
[7] D.L.Y. Kong, J.G. Sanjayan, Effect of elevated temperatures on geopolymer paste, mortar and concrete, Cem. Concr. Res. 40 (2) (2010) 334–339, https://doi.org/10.1016/j.cemconres.2009.10.017.
[8] A. Hajimohammadi, J.L. Provis, J.S.J. van Deventer, One-part geopolymer mixes from geothermal silica and sodium aluminate, AIChE Annu. Meet. Conf. Proc. 47 (23) (2008) 9396–9405.
[9] T. Luukkonen, Z. Abdollahnejad, J. Yliniemi, P. Kinnunen, M. Illikainen, One-part alkali-activated materials: A review, Cem. Concr. Res. 103 (2018) 21–34, https://doi.org/10.1016/j.cemconres.2017.10.001.
[10] T. Luukkonen, Z. Abdollahnejad, J. Yliniemi, P. Kinnunen, M. Illikainen, Comparison of alkali and silica sources in one-part alkali-activated blast furnace slag mortar, J. Clean. Prod. 187 (2018) 171–179, https://doi.org/10.1016/j.jclepro.2018.03.202.
[11] S.A. Bernal, R. Mejía De Gutiérrez, J.L. Provis, Engineering and durability properties of concretes based on alkali-activated granulated blast furnace slag/metakaolin blends, Constr. Build. Mater. 33 (2012) 99–108, https://doi.org/10.1016/j.conbuildmat.2012.01.017.
[12] Z. Abdollahnejad, F. Pacheco-Torgal, J.B. Aguiar, C. Jesus, Durability Performance of Fly Ash Based One-Part Geopolymer Mortars, Key Eng. Mater. 634 (2015) 113–120, https://doi.org/10.4028/www.scientific.net/KEM.634.113.
[13] F. Collins, J.G. Sanjayan, Cracking tendency of alkali-activated slag concrete subjected to restrained shrinkage, Cem. Concr. Res. 30 (5) (2000) 791–798, https://doi.org/10.1016/S0008-8846(00)00243-X.
[14] S. Aydın, B. Baradan, The effect of fiber properties on high performance alkali-activated slag/silica fume mortars, Compos Part B Eng 45 (1) (2013) 63–69, https://doi.org/10.1016/j.compositesb.2012.09.080.
[15] F. Puertas, T. Amat, A. Fernández-Jiménez, T. Vázquez, Mechanical and durable behaviour of alkaline cement mortars reinforced with polypropylene fibres, Cem. Concr. Res. 33 (12) (2003) 2031–2036, https://doi.org/10.1016/S0008-8846(03)00222-9.
[16] Z. Abdollahnejad, M. Mastali, B. Woof, M. Illikainen, High strength fiber reinforced one-part alkali activated slag/fly ash binders with ceramic aggregates: Microscopic analysis, mechanical properties, drying shrinkage, and freeze-thaw resistance, Constr. Build. Mater. 241 (2020) 118129, https://doi.org/10.1016/j.conbuildmat.2020.118129.
[17] F.J. Silva, C. Thaumaturgo, Fibre reinforcement and fracture response in geopolymeric mortars, Fatigue Fract. Eng. Mater. Struct. 26 (2) (2003) 167–172, https://doi.org/10.1046/j.1460-2695.2003.00625.x.
[18] Ü. Yurt, An experimental study on fracture energy of alkali activated slag composites incorporated different fibers, J. Build. Eng. 32 (2020) 101519, https://doi.org/10.1016/j.jobe.2020.101519.
[19] S.F.U. Ahmed, H. Mihashi, A review on durability properties of strain hardening fibre reinforced cementitious composites (SHFRCC), Cem. Concr. Compos. 29 (5) (2007) 365–376, https://doi.org/10.1016/j.cemconcomp.2006.12.014.
[20] A. Bentur, S. Mindess, Fibre Reinforced Cementitious Composites, 2nd ed., CRC Press, 1990. Doi: 10.1201/9781482267747.
[21] M. Abdulkareem, J. Havukainen, M. Horttanainen, How environmentally sustainable are fibre reinforced alkali-activated concretes? J. Clean. Prod. 236 (2019) 117601, https://doi.org/10.1016/j.jclepro.2019.07.076.
[22] M. Nedeljković, M. Luković, K. van Breugel, D. Hordijk, G. Ye, Development and application of an environmentally friendly ductile alkali-activated composite, J. Clean. Prod. 180 (2018) 524–538, https://doi.org/10.1016/j.jclepro.2018.01.162.
[23] M.M. Al-mashhadani, O. Canpolat, Y. Aygörmez, M. Uysal, S. Erdem, Mechanical and microstructural characterization of fiber reinforced fly ash based geopolymer composites, Constr. Build. Mater. 167 (2018) 505–513, https://doi.org/10.1016/j.conbuildmat.2018.02.061.
[24] M.H. Al-Majidi, A. Lampropoulos, A.B. Cundy, Tensile properties of a novel fibre reinforced geopolymer composite with enhanced strain hardening characteristics, Compos. Struct. 168 (2017) 402–427, https://doi.org/10.1016/j.compstruct.2017.01.085.
[25] X. Guo, X. Pan, Mechanical properties and mechanisms of fiber reinforced fly ash–steel slag based geopolymer mortar, Constr. Build. Mater. 179 (2018) 633–641, https://doi.org/10.1016/j.conbuildmat.2018.05.198.
[26] L. Kan, R. Shi, Y. Zhao, X. Duan, M. Wu, Feasibility study on using incineration fly ash from municipal solid waste to develop high ductile alkali-activated composites, J Clean Prod 254 (2020) 120168, https://doi.org/10.1016/j.jclepro.2020.120168.
[27] T. Alomayri, Effect of glass microfibre addition on the mechanical performances of fly ash-based geopolymer composites, J. Asian Ceram. Soc. 5 (3) (2017) 334–340, https://doi.org/10.1016/j.jascer.2017.06.007.
[28] P. Behera, V. Baheti, J. Militky, P. Louda, Elevated temperature properties of basalt microfibril filled geopolymer composites, Constr. Build. Mater. 163 (2018) 850–860, https://doi.org/10.1016/j.conbuildmat.2017.12.152.
[29] S. Yan, P. He, D. Jia, Z. Yang, X. Duan, S. Wang, Y.u. Zhou, Effect of fiber content on the microstructure and mechanical properties of carbon fiber felt reinforced geopolymer composites, Ceram. Int. 42 (6) (2016) 7837–7843, https://doi.org/10.1016/j.ceramint.2016.01.197.
[30] H.A. Santana, N.S. Amorim Júnior, D.V. Ribeiro, M.S. Cilla, C.M.R. Dias, Vegetable fibers behavior in geopolymers and alkali-activated cement based matrices: A review, J Build Eng 44 (2021) 103291, https://doi.org/10.1016/j.jobe.2021.103291.
[31] A. Adesina, Performance of fibre reinforced alkali-activated composites – A review, Materialia 12 (2020) 100782, https://doi.org/10.1016/j.mtla.2020.100782.
[32] A. Niş, N.A. Eren, A. Çevik, Effects of nanosilica and steel fibers on the impact resistance of slag based self-compacting alkali-activated concrete, Ceram. Int. 47 (17) (2021) 23905–23918, https://doi.org/10.1016/j.ceramint.2021.05.099.
[33] Z. Abdollahnejad, M. Mastali, M. Falah, K.M. Shaad, T. Luukkonen, M. Illikainen, Durability of the Reinforced One-Part Alkali-Activated Slag Mortars with Different Fibers, Waste Biomass Valorization 12 (1) (2021) 487–501, https://doi.org/10.1007/s12649-020-00958-x.
[34] Z. Abdollahnejad, M. Mastali, T. Luukkonen, P. Kinnunen, M. Illikainen, Fiber-reinforced one-part alkali-activated slag/ceramic binders, Ceram. Int. 44 (8) (2018) 8963–8976, https://doi.org/10.1016/j.ceramint.2018.02.097.
[35] S.F.A. Shah, B. Chen, S.Y. Oderji, M. Aminul Haque, M.R. Ahmad, Comparative study on the effect of fiber type and content on the performance of one-part alkali-activated mortar, Constr. Build. Mater. 243 (2020) 118221, https://doi.org/10.1016/j.conbuildmat.2020.118221.
[36] A.H.M. Andreasen, J. Andersen, On the relationship of particle gradation and void content of products made of loose granular mixtures (including few experiments), Kolloid 50 (1930) 217–228.
[37] P. Perumal, H. Sreenivasan, T. Luukkonen, A.M. Kantola, V.-V. Telkki, P. Kinnunen, M. Illikainen, High strength one-part alkali-activated slag blends designed by particle packing optimization, Constr. Build. Mater. 299 (2021) 124004, https://doi.org/10.1016/j.conbuildmat.2021.124004.
[38] T. Luukkonen, Z. Abdollahnejad, K. Ohenoja, P. Kinnunen, M. Illikainen, Suitability of commercial superplasticizers for one-part alkali-activated blast-furnace slag mortar, J. Sustain Cem. Mater. 8 (4) (2019) 244–257, https://doi.org/10.1080/21650373.2019.1625827.
[39] Rilem. Determination of the fracture energy of mortar and concrete by means of three-point bend tests on notched beams. Mater. Struct. 1985;18:287–90. Doi: 10.1007/BF02472918.
[40] H. Nguyen, P. Kinnunen, V. Carvelli, M. Mastali, M. Illikainen, Strain hardening polypropylene fiber reinforced composite from hydrated ladle slag and gypsum, Compos Part B Eng 158 (2019) 328–338, https://doi.org/10.1016/j.compositesb.2018.09.056.
[41] LaVision. LaVision StrainMaster 2016. https://www.lavision.de/en/products/strainmaster/ (accessed July 16, 2021).
[42] S. Bernal, R. De Gutierrez, S. Delvasto, E. Rodriguez, Performance of an alkali-activated slag concrete reinforced with steel fibers, Constr. Build. Mater. 24 (2) (2010) 208–214, https://doi.org/10.1016/j.conbuildmat.2007.10.027.
[43] B. Wei, H. Cao, S. Song, Tensile behavior contrast of basalt and glass fibers after chemical treatment, Mater. Des. 31 (9) (2010) 4244–4250, https://doi.org/10.1016/j.matdes.2010.04.009.
[44] V. Dhand, G. Mittal, K.Y. Rhee, S.J. Park, D. Hui, A short review on basalt fiber reinforced polymer composites, Compos Part B Eng 73 (2015) 166–180, https://doi.org/10.1016/j.compositesb.2014.12.011.
[45] S.T. Bashir, L. Yang, J.J. Liggat, J.L. Thomason, Kinetics of dissolution of glass fibre in hot alkaline solution, J. Mater. Sci. 53 (3) (2018) 1710–1722, https://doi.org/10.1007/s10853-017-1627-z.
[46] S.R. Gislason, E.H. Oelkers, Mechanism, rates, and consequences of basaltic glass dissolution: II. An experimental study of the dissolution rates of basaltic glass as a function of pH and temperature, Geochim. Cosmochim. Acta 67 (2003) 3817–3832, https://doi.org/10.1016/S0016-7037(00)00176-5.
[47] D.Y. Yoo, S.T. Kang, Y.S. Yoon, Effect of fiber length and placement method on flexural behavior, tension-softening curve, and fiber distribution characteristics of UHPFRC, Constr. Build. Mater. 64 (2014) 67–81, https://doi.org/10.1016/j.conbuildmat.2014.04.007.
[48] D.Y. Yoo, N. Banthia, Mechanical properties of ultra-high-performance fiber-reinforced concrete: A review, Cem. Concr. Compos. 73 (2016) 267–280, https://doi.org/10.1016/j.cemconcomp.2016.08.001.
[49] Dussault Systemes Simulia. Abaqus/CAE User's Manual. vol. IV; 2019.
[50] Chu DJC, K-H. Stress-Strain Relationship for Plain Concrete in Compression. ACI J Proc n.d.;82. Doi: 10.14359/10390.

[51] M. di Prisco, M. Colombo, D. Dozio, Fibre-reinforced concrete in fib Model Code 2010: Principles, models and test validation, Struct. Concr. 14 (4) (2013) 342–361, https://doi.org/10.1002/suco.v14.410.1002/suco.201300021.
[52] V. Carvelli, A. Veljkovic, H. Nguyen, A. Adediran, P. Kinnunen, N. Ranjbar, M. Illikainen, Low-velocity impact of hot-pressed PVA fiber-reinforced alkali-activated stone wool composites, Cem. Concr. Compos. 114 (2020) 103805, https://doi.org/10.1016/j.cemconcomp.2020.103805.
[53] S.-T. Kang, Y. Lee, Y.-D. Park, J.-K. Kim, Tensile fracture properties of an Ultra High Performance Fiber Reinforced Concrete (UHPFRC) with steel fiber, Compos. Struct. 92 (1) (2010) 61–71, https://doi.org/10.1016/j.compstruct.2009.06.012.
[54] fib Model Code for Concrete Structures 2010. Verlag GmbH & Co. KGaA, Weinheim, Germany: 2013. Doi: 10.1002/9783433604090.